Single-cell characterization of deformation and dynamics of mesenchymal stem cells in microfluidic systems: A computational study

Xiaojing Qi [1], Shuhao Ma [1], Xinchi Jiang [2,*], Honghui Wu,[2] Juanjuan Zheng,[2] Shuo Wang [1], Keqin Han,[1] Tianyuan Zhang [2], Jianqing Gao,[2,†] and Xuejin Li [1,‡]

[1]*Department of Engineering Mechanics and Center for X-Mechanics, Zhejiang University, Hangzhou 310027, China*
[2]*College of Pharmaceutical Sciences, Zhejiang University, Hangzhou 310027, China*

Understanding the homing dynamics of individual mesenchymal stem cells (MSCs) in physiologically relevant microenvironments is crucial for improving the efficacy of MSC-based therapies for therapeutic and targeting purposes. This study investigates the passive homing behavior of individual MSCs in micropores that mimic interendothelial clefts through predictive computational simulations informed by previous microfluidic experiments. Initially, we quantified the size-dependent behavior of MSCs in micropores and elucidated the underlying mechanisms. Subsequently, we analyzed the shape deformation and traversal dynamics of each MSC. In addition, we conducted a systematic investigation to understand how the mechanical properties of MSCs impact their traversal process. We considered geometric and mechanical parameters, such as reduced cell volume, cell-to-nucleus diameter ratio, and cytoskeletal prestress states. Furthermore, we quantified the changes in the MSC traversal process and identified the quantitative limits in their response to variations in micropore length. Taken together, the computational results indicate the complex dynamic behavior of individual MSCs in the confined microflow. This finding offers an objective way to evaluate the homing ability of MSCs in an interendothelial-slit-like microenvironment.

I. INTRODUCTION

Numerous clinical trials have examined the efficacy of adult mesenchymal stem cells (MSCs) or multipotent stromal cells in the treatment of tissues damaged by inflammation or conditions such as cardiovascular disease, myocardial infarction, brain and spinal cord injury, stroke, and diabetes [1,2]. Animal-based preclinical studies have shown that MSCs injected into the vascular circulation migrate preferentially to the inflamed or ischemic tissue, which is fundamental to their efficacy [3,4]. Despite the intravenous injection of MSCs, one of the major challenges in MSC-based therapies is the lack of delivery of MSCs to inflamed or ischemic tissues, which is a process known as "homing" [3,5,6]. It is still unclear whether the administered MSCs actively migrate to sites of inflammation by leukocytelike transendothelial migration mechanisms [refer to Fig. 1(a)] or passively get trapped in microvessels [3]. Nevertheless, the exit of MSCs from the vascular circulation is a critical mechanism for their homing to specific sites. This dynamic process requires MSCs to pass through the interendothelial clefts (IECs) between endothelial cells, which is a small but open gap as narrow as 2 µm in size [8].

The ability of circulating cells, including MSCs and blood cells, to pass through narrow blood vessels such as IECs and interendothelial slits (IESs) is essential for their biological functions and clinical implications [10–12]. The identification, detection, and characterization of circulating cells at the single-cell level are complicated processes. Therefore, understanding cell traversal activity through narrow passages within *in vivo* systems is still challenging. Microfluidics, which allows precise control of the mechanical and chemical environment around living cells, is a powerful technology for studying cell behaviors at the single-cell to multicell level [13–19]. In recent decades, researchers have investigated the movement of blood cells through narrow spaces with diameters smaller than the size of the cells [20–27]. For instance, Shelby *et al.* carried out a microfluidic test on both healthy and malaria-infected red blood cells (RBCs) to evaluate their ability to pass through constrictions with diameters of 8, 6, 4, and 2 microns [20]. The results showed that healthy RBCs could easily pass through all constrictions. In contrast, RBCs infected with late-stage malaria were unable to pass through constrictions as small as 6 µm or even narrower, leading to the formation of blockages in the capillaries. Quinn and colleagues conducted a study of the biophysical properties of healthy RBCs passing through microfluidic channels with cross-sectional areas as small as $2.7 \, \mu m \times 3 \, \mu m$ [22]. The study identified a critical cross-sectional area below which the dynamic flow behavior of RBCs at room temperature is dominated by their membrane properties. Du *et al.* developed a microfluidic device that controls oxygen pressure to investigate sickle cell behavior under transient hypoxia. The kinetics of sickle cell biorheology were quantified by measuring patient-specific blood samples using this microfluidic device [25]. Papageorgiou *et al.* quantified the simultaneous and

*Corresponding author: 11419014@zju.edu.cn
†Corresponding author: gaojianqing@zju.edu.cn
‡Corresponding author: xuejin_li@zju.edu.cn
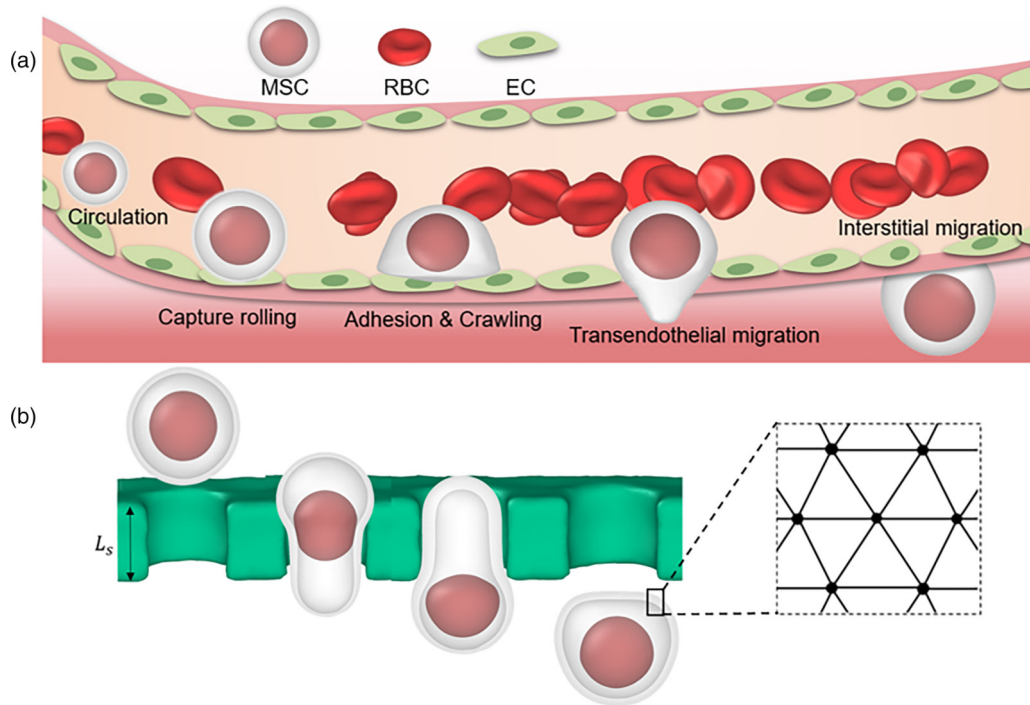
FIG. 1. (a) Schematic representation of the homing process of an individual MSC. In blood vessels, MSC homing occurs through four processes: (1) capture rolling, (2) adhesion and crawling, (3) transendothelial migration, and (4) interstitial migration. (b) A sketch of the simulation model of the MSC passing through the micropore (see Video S1 in the Supplemental Material [7]). In this model, the whole MSC model consists of the MSC membrane (white) and the MSC nucleus (red), and the IEC-like micropore is shown in green. The diameters of the whole MSC and its nucleus are $D_{\mathrm{MSC}} = 15.8\,\mu\mathrm{m}$ and $D_{\mathrm{Nucelus}} = 9.75\,\mu\mathrm{m}$, respectively, according to the measured data in the available experiment [9]; the diameter of the micropore, D_{pore}, is changed in the range from 5.8 to 14.0 μm.

synergistic effects of RBC adhesion and sickle hemoglobin polymerization on the mechanisms underlying vaso-occlusive pain crisis using a hypoxic microfluidic RBC adhesion assay [26]. They found that the age of RBCs in circulation plays a critical role in mediating the synergistic effect on blood rheology and clinical symptoms. In addition, microfluidic platforms were used to study the dynamics of white blood cell (WBC) passage through narrow channels [28–30]. For example, Schreiber *et al.* utilized a Transwell-based microfluidic chamber to study WBC transmigration through a porous filter under hemodynamic shear conditions [31]. Their study showed that the physiological shear flow during WBC transmigration leads to combinatorial responses to sequential heterologous chemokine signals. Downey *et al.* investigated the blockage of microcapillaries by WBCs and found that the differential WBC retention in the lung is determined by the biophysical features of cell size and deformability [32]. More recently, Sormendi and colleagues conducted a study on the migration of neutrophils through high-confinement microenvironments [33]. They found that the overactivation of hypoxia-inducible factor 2 can enhance neutrophil migration even in highly confined environments. The investigations of the transit of blood cells through restricted geometries provide important insights into the journey of an MSC through the IEC [8,9,34].

To gain a better understanding of the characteristic behavior of individual MSCs, microfluidic experiments were performed *in vitro* to investigate the homing dynamics

and entrapment mechanisms in IEC-like microenvironments [9,35,36]. For example, real-time deformability cytometry (RT-DC), a microfluidic technique for characterizing cell mechanics, has the potential for label-free dose-response assays based on high-throughput cell mechanical phenotypes in a single run [9,35,36]. Xavier *et al.* employed the RT-DC microfluidic device to differentiate between skeletal stem cells (a subpopulation of MSCs) and cancer cells [35]. Lipowsky *et al.* demonstrated pressure-driven filtration of MSCs through porous filters using a transient filtration assay [9]. The MSC nucleus contributed significantly to its resistance to deformation during the transmigration process.

In addition to microfluidic experimental studies, the recent developments of computational modeling and simulation enable the investigation of various mechanical, rheological, and dynamic problems associated with circulating cells [29, 37–45]. For instance, Freund *et al.* employed a boundary integral model (BIM) to simulate the flow dynamics of isolated RBCs through the splenic IESs [46]. During the RBC traversal process, they identified three distinctive behaviors based on the flow rate and cytosol viscosity. Lu and Peng integrated the BIM with a spectrin-linked RBC model to examine the cell traversal dynamics through the splenic IES [47]. The study investigated the effects of pressure difference, surface-area-to-volume ratio, and membrane stiffness on the RBCs' deformation and internal stress. Pivkin *et al.* developed a unique quantitative framework based on dissipative particle dynamics (DPD) to investigate the circulating RBCs cross-

ing the splenic IES [48]. They identified quantitative limits for splenic IES clearances. Li *et al.* simulated RBC traversal of the splenic IES and revealed that vesiculation of the RBC membrane may cause membrane surface loss during the process [49].

The migration of cells through narrow passages is a crucial step in the circulation process. The process is influenced by the structural and mechanical properties of the cells, as well as the size of the passage. Quantifying the morphological and mechanical factors involved in cell passage dynamics using current microfluidic experimental studies alone is challenging. Accurate computational modeling, combined with microfluidic experiments, can provide valuable information about the complex behavior of circulating cells during their traversal through narrow passages. For example, Bow *et al.* utilized a microfluidic device with periodic obstacles to blood flow to characterize the biomechanical properties of malaria-infected RBCs [21]. Experimental measurements were converted into quantitative data describing the mechanical characteristics of individual RBCs using a mesoscopic RBC model. The simulations precisely captured the impact of changes in RBC properties induced by parasitization on the movement of healthy and malaria-infected RBCs. Li *et al.* conducted a study of the complex behavior of individual sickle RBCs in a microenvironment similar to a microcapillary using dynamic microfluidic experiments and multiscale simulations [50]. The study clarified how changes in cell deformability and volume impact the dynamic behavior of individual sickle RBCs and their involvement in single-cell capillary obstruction. This information could aid in evaluating the effectiveness of targeted drug therapy for the alleviation or prevention of vaso-occlusive crisis.

In this study, we employ a comparable approach to investigate the dynamics of individual MSC traversal in an IES-like microenvironment through predictive computational simulations informed by relevant microfluidic experiments. We investigate the functional relationship between the relative filtration pressure (P) and the ratio of MSC-to-micropore diameter (λ) and examine the mechanisms underlying the λ dependence of the relative filtration pressure P. Subsequently, we examine the effect of the cellular nucleus on the dynamics of MSC traversal. Furthermore, we analyze the shape deformation and traversal dynamics of individual MSCs as they pass through the IEC-like microenvironment. Additionally, we conduct a systematic investigation to understand how the mechanical properties of the MSCs impact their traversal process. We also quantify the structural and mechanical factors of MSC traversal and entrapment.

II. MODELS AND METHODS

In this study, numerical simulations are performed to investigate the mechanical properties and deformation behavior of MSCs during cell transmigration.

A. Model formulations of dissipative particle dynamics

Dissipative particle dynamics (DPD) is a coarse-grained mesoscopic method that uses coarse-grained descriptions in which groups of atoms are treated as a unit [51,52]. A DPD

particle represents a cluster of molecules rather than individual atoms, and the position and momentum of the particle are updated in continuous phases but spaced at discrete time steps. The interacting force imposed on a DPD particle i is the sum of the pairwise conservative force ($\mathbf{F}_{ij}^{C}$), dissipative force ($\mathbf{F}_{ij}^{D}$), and random force ($\mathbf{F}_{ij}^{R}$) via interactions with the particle j within a radial cutoff r_c. Typical forms of these three pairwise forces are given by [51–53]

$$\mathbf{F}_{ij}^{C} = a_{ij}\omega^{C}(r_{ij})\mathbf{e}_{ij}, \tag{1}$$

$$\mathbf{F}_{ij}^{D} = -\gamma_{ij}\omega^{D}(r_{ij})(\mathbf{e}_{ij} \cdot \mathbf{v}_{ij})\mathbf{e}_{ij}, \tag{2}$$

$$\mathbf{F}_{ij}^{R} = \sigma_{ij}\omega^{R}(r_{ij})\xi_{ij}\Delta t^{-1/2}\mathbf{e}_{ij}, \tag{3}$$

where $\mathbf{v}_{ij}$ is the difference between two velocities $\mathbf{v}_i$ and $\mathbf{v}_j$, $\mathbf{e}_{ij} = \frac{\mathbf{r}_{ij}}{r_{ij}}$ is the unit vector from particles i and j, and ξ_{ij} is a symmetric Gaussian random variable with zero mean and unit variance. The coefficients a_{ij}, γ_{ij}, and σ_{ij} define, respectively, the interaction strengths of conservative, dissipative, and random forces, and $\omega^{C}(r_{ij})$, $\omega^{D}(r_{ij})$, and $\omega^{R}(r_{ij})$ are the corresponding weight functions. Specifically, the choice for the weight functions is as follows:

$$\omega^{C} = (1 - r_{ij}/r_c)^m, \quad r_{ij} \leqslant r_c \tag{4}$$

$$\omega^{D}(r_{ij}) = [\omega^{R}(r_{ij})]^2 = \left(1 - \frac{r_{ij}}{r_c}\right)^{2k}, \quad r_{ij} \leqslant r_c, \tag{5}$$

where m and k are the exponents of the DPD envelope. Here, we choose $m = 0.25$ and $k = 0.25$ to increase the viscosity of the DPD fluid. In past decades, the DPD method and its extensions have been successfully applied to study the behavior of physical and biological systems [39,41,42,54], including biological cell membranes [55,56], droplet suspension [57,58], and blood flow [59–64].

B. Mesoscopic model of individual MSC

The modeling framework of the MSC is similar to those of the RBCs and WBCs, which have been tested against the cell mechanics, dynamics, and rheology of a variety of experiments and have successfully explored the margination and adhesion dynamics in microcapillary flow [49,60,61, 65–67]. Specifically, the energy of the viscoelastic cell membrane model is defined using four parts: the elastic energy (E_s), the bending resistance (E_b), and the surface area (E_{area}) and volume (E_{volume}) constraints,

$$E = E_s + E_b + E_{area} + E_{volume}, \tag{6}$$

where E_s and E_b are determined by

$$E_s = \sum_{i \in \text{springs}} \left[\frac{k_B T l_m (3x_i^2 - 2x_i^3)}{4p(1 - x_i)} + \frac{k_p}{(n-1)l_i^{n-1}} \right], \tag{7}$$

$$E_b = \sum_{i \in \text{springs}} k_b [1 - \cos(\theta_i - \theta_0)]. \tag{8}$$

where p is the persistence length, $k_B T$ is the energy unit, n is an exponent, $x_i = \frac{l_i}{l_m}$, l_m is the maximum length extension, and l_i is the length of the spring i. In Eq. (8), k_b is the bending constant, which can be related to the macroscopic bending rigidity k_c of the Helfrich curvature-elasticity model by the

TABLE I. Parameters of MSC membrane and MSC nucleus models used in DPD simulations. A_0 and V_0 are surface area and volume, respectively. μ_0 and k_c are shear modulus and bending stiffness.

Model	D (μm)	A_0 (μm^2)	V_0 (μm^3)	μ_0 (pN μm^{-1})	k_c ($10^{-19}J$)
MSC membrane	15.80	784.3	2065.2	4.7	2.4
MSC nucleus	9.75	298.6	485.3	47.0	2.4

TABLE II. Selected parameters used in DPD simulations. a_{ij} and γ_{ij} are the coefficients of the DPD conservative and dissipative forces, r_c is the cutoff radius, k is the exponent of the DPD envelope, symbols F and W indicate fluid and wall particles, and M and N represent the particles on the MSC membrane and cellular nucleus, respectively.

Interaction	a_{ij}	γ_{ij}	r_c	k
F-F/F-W/F-M/F-N/M-N	25.0	30.0	1.0	0.25
W-M	50.0	30.0	1.5	0.25
W-N	50.0	30.0	1.0	0.25

equation $k_b = \frac{2}{\sqrt{3}}k_c$ [68,69]. θ_i and θ_0 are the instantaneous and spontaneous angles between two adjacent triangles sharing common edge i.

Furthermore, constraints are imposed on the area and volume conservation of the MSC to mimic the characteristics of an area-preserving cell membrane and incompressible internal fluid, which is expressed as

$$E_{\text{area}} = \sum_{j\in\text{triangles}} \frac{k_d(A_j - A_{j,0})^2}{2A_{j,0}} + \frac{k_a(A - A_0)^2}{2A_0}, \quad (9)$$

$$E_{\text{volume}} = \sum_{j\in\text{triangles}} \frac{k_v(V - V_0)^2}{2V_0}, \quad (10)$$

where k_a, k_d, and k_v denote the global area, local area, and volume constraint coefficients, respectively. A_0 and V_0 are the total area and volume of the MSC membrane at equilibrium. Additionally, the term $A_{j,0}$ represents the area of the triangle j. According to the theoretical analysis conducted on a regular hexagonal network by Dao *et al.*, the membrane shear modulus can be determined as follows:

$$\mu = \frac{\sqrt{3}k_B T}{4pl_m x_0}\left[\frac{x_0}{2(1-x_0)^3} - \frac{1}{4(1-x_0)^2} + \frac{1}{4}\right]$$
$$+ \frac{\sqrt{3}k_p(\nu+1)}{4l_0 + 1}, \quad (11)$$

where l_0 is the equilibrium length of the spring and $x_0 = l_0/l_m$.

In the current study, the computational MSC model is constructed by considering their shape and mechanical characteristics [9,70]. For instance, previous experiments have shown that MSCs have spherical shapes with a mean diameter of around 15.8 μm [9]. The modeled MSC is a triangulated sphere with a diameter of 15.8 μm. Moreover, the MSC nucleus is stiffer than its membrane, which is similarly represented as a triangulated sphere with a diameter of 9.75 μm; see Fig. 1(b). According to experimental measurements, the stiffness of the MSC nucleus is 2 to 10 times higher than that of the MSC membrane [71–74]. Therefore, the shear modulus of the modeled MSC nucleus is assumed to be 10 times greater than that of the MSC membrane. Table I lists the selected parameters of the MSC models used in the DPD simulation. As mentioned in Sec. III, the micropores are cylinders with different diameters based on the experiments of Lipowsky *et al.* [9].

A modified version of LAMMPS [75], with a time step $\Delta t = 0.883$ ms, performs all simulations. A typical simulation requires about 8.0×10^5 time steps and consumes approximately 64 CPU core hours, using computational resources

such as Intel E5-2680 2.5 GHz 24-core processors at the Beijing Super Cloud Computing Center (BLSC).

III. RESULTS AND DISCUSSION

A. Validation of DPD fluid flow in microfluidic channels

Controlling the particle density fluctuations of fluid particles with soft DPD interactions is technically challenging due to the potential compressibility issues that may arise in DPD simulations. In this study, we model the fluid flow to meet the no-slip boundary condition and achieve the prescribed particle density by implementing the following strategies: (1) To avoid the particle interpenetration issue seen in the original DPD method, as proposed by previous computational studies [76,77], a rigid core is included in each DPD particle by modifying the weight function ω^C of the conservative force [see Eq. (4)]. Table II summarizes the repulsive parameters for the interaction between two DPD particles, including fluid (F) and wall (W) particles. A typical conservative force curve used in this study is shown in Fig. S1 in the Supplemental Material [7]. This approach mostly prevents the overlapping of soft DPD particles, an issue in the original DPD model. (2) An additional bounce-back rule is applied to prevent MSC and fluid particles from entering the solid wall domain. The rule reflects the velocity of a DPD particle colliding with the wall back into the fluid channel.

A simulation of a single-phase flow is performed to validate the fluid flow in the microfluidic channel. As shown in Fig. S2 in the Supplemental Material [7], the microfluidic channel (green particles) is filled with fluid particles (cyan particles). A narrow cylindrical channel was created in the center of the microfluidic channel, with a length of $L = 11$ μm and a diameter of $d = 11$ μm. Two symmetrical wide channels were created at the top and bottom of the narrow channel. The microfluidic channel walls were formed using stationary DPD particles, and impermeable and no-slip boundary conditions were applied at the fluid-solid boundary using bounce-back reflections and the appropriate dissipative forces. The density profiles of the fluid particles obtained from the DPD simulation are shown in Fig. S2 (see Supplemental Material [7]). The particle density profiles perpendicular to the flow direction show a uniform distribution, except for statistical fluctuations. Thus, the modified DPD method prevents the possible occurrence of particle density artifacts. Next, we computed the two-dimensional velocity contours within the y-z plane using DPD and continuum simulations, as shown in Fig. S3
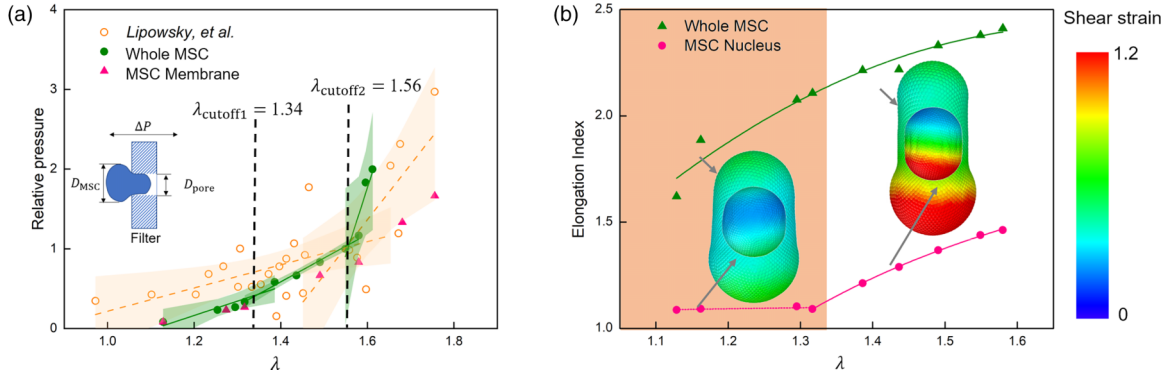
FIG. 2. (a) Quantitative prediction of the relative filtration pressure and elongation index of individual MSCs as a function of the λ ratio. Results are compared with available experimental data [9]. Green circles and pink triangles represent the computational data for the whole MSC and the MSC membrane (excluding the MSC nucleus). The yellow circles depict the associated experimental data, and the orange dashed lines represent the line segments that fit linearly in previous experimental study [9]. Linear regression of the whole MSC is displayed above and below the λ_{cutoff}. The value was obtained iteratively by identifying the intersection of the best linear fits. Shadow region represents the 95% confidence interval. (b) The functional dependence of the elongation index of the whole MSC (and the MSC nucleus) on the λ ratio.

(see Supplemental Material [7]). The velocity contours, except in the narrow domain, illustrate negligible differences between the continuum and DPD solvers. We then calculated the velocity profile of fluid particles obtained from DPD simulations by considering the cross-flow direction at station P2. Figure S3 (see Supplemental Material [7]) compares the results of continuum simulations (COMSOL) and DPD simulations. Although there are slight variations in the velocity profiles, the relative mean-square difference of the maximum velocities between the DPD and continuum results at station P2 is less than 2.65%, which is negligible to a significant extent. Therefore, the modified approach can be effectively used for fluid flow.

B. Dynamics of the MSC traversal through circular micropores

Techniques for transient filtration developed from micropipette aspiration have demonstrated the ability to illustrate the heterogeneity of cell properties, as exemplified in previous studies [9,32,78]. In the transient filtration test of MSCs, as shown in the inset of Fig. 2(a), the diameter ratio between the MSC and micropore is calculated as $\lambda = \frac{D_{\text{MSC}}}{D_{\text{pore}}}$, with D_{MSC} and D_{pore} representing the respective diameters of the whole MSC and the micropore. In a previous study, Lipowsky *et al.* [9] investigated the functional dependence between the relative filtration pressure P and the λ ratio during the MSC traversal, represented as yellow circles in Fig. 2(a). A linear fit analysis with a critical value of $\lambda_{\text{cutoff2}} = 1.56$ divided the $P - \lambda$ curve into two segments, each resulting in linear regressions above and below the λ_{cutoff2} value; see the orange dashed lines in Fig. 2(a). Nevertheless, the linear correlation between these two sections is weak, and the influence of the MSC nucleus and MSC membrane on the functional dependence of P on the λ ratio remains uncertain. We conducted simulations of transient filtration tests of the MSCs at various levels of P to quantify the effect of the MSC nucleus on their traversal dynamics at different micropore sizes.

Figure 2(a) illustrates the functional dependence of P on the λ ratio for the whole MSC. According to the simulation data, we segment the P - λ curve into three parts for numerical analysis in the following manner:

(1) $P = 1.80\lambda - 1.99$, $\lambda < \lambda_{\text{cutoff1}}$
(2) $P = 2.98\lambda - 3.59$, $\lambda_{\text{cutoff1}} \leqslant \lambda < \lambda_{\text{cutoff2}}$
(3) $P = 16.93\lambda - 25.32$, $\lambda \geqslant \lambda_{\text{cutoff2}}$.

The simulation results indicate a reasonable linearity between P and the ratio of λ, particularly for low λ ratios (i.e., $\lambda < \lambda_{\text{cutoff2}}$), which is consistent with previous experimental studies [9]. In contrast to the experimental findings, we also conducted computational simulations of the traversal dynamics of the pure MSC membrane (excluding the MSC nucleus). Thus, two sets of λ_{cutoff} values exist. When $\lambda < \lambda_{\text{cutoff1}}$, the P - λ ratios of the whole MSC and the pure membrane are almost equal, pointing to the negligible impact of the cellular nucleus on the traversing process at this stage. When $\lambda \geqslant \lambda_{\text{cutoff2}}$, the relative filtration pressure required for the whole MSC to pass through the micropores increases rapidly, at a much higher rate than the relative pressure required for the passage of the pure MSC membrane, suggesting that the cellular nucleus is the major limiting factor for its passage.

C. Shape deformation of the MSC during its traversal through circular micropores

Next, we investigate the elastic deformation of MSCs to quantify cell shape deformation during the traversal process. In this study, the elastic deformation of individual MSCs is expressed as an elongation index (EI) defined by $\text{EI} = \frac{D_A}{D_T}$, where D_A and D_T represent the major and minor axes of the deformed MSC. Figure 2(b) shows the relationship between the EI values of the whole MSC (and the MSC nucleus) and the λ ratio. It can help to understand the three-segment piecewise linear function curve shown in Fig. 2(a): (1) For $\lambda < \lambda_{\text{cutoff1}}$, the MSC nucleus is almost unaffected, indicating that the resistance of the MSC to pass through the micropore comes mainly from the pure MSC membrane. (2) For λ between λ_{cutoff1} and λ_{cutoff2}, the MSC nucleus begins to deform, requiring a more significant P to drive the whole MSC to pass through the micropore. At this stage, both the MSC membrane and the MSC nucleus would influence the entire MSC
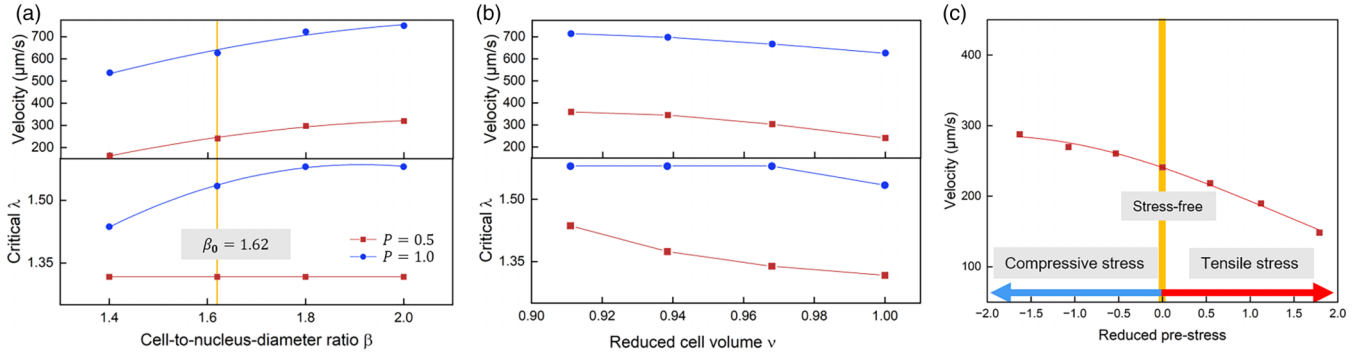
FIG. 3. The correlation between MSC transit velocity and cell mechanical properties under relative pressure differences of $P = 0.5$ (red squares) and 1.0 (blue circles). (a) The correlation between MSC transit velocity (along with critical λ ratio) and cell-to-nucleus diameter ratio. (b) The functional relationship between MSC transit velocity (along with critical λ ratio) and the reduced cell volume ν. (c) The correlation between MSC transit velocity and cell prestress states at a relative pressure difference of $P = 0.5$ (red squares). The reduced prestress value is obtained by dividing the physical prestress by a specific value of $\tau_s = -0.60$ pN μm (corresponding to the shear stress when the MSC is at its maximum deformation state at $P = 0.5$). Negative values of reduced prestress indicate that the MSC is subject to compressive stress and is compressed, whereas positive values suggest that the MSC is stretched. Please refer to Fig. S4 in the Supplemental Material [7] for more information. In the figures, the critical ratio of λ represents the ratio between the diameter of MSC and the minimum diameter of the micropore that MSC can pass under a specific pressure difference.

traversal process. (3) For $\lambda \geqslant \lambda_{\text{cutoff2}}$, the size of the MSC nucleus, D_{nucleus}, is larger than the size of the micropore, D_{pore}. Therefore, it is difficult for the whole MSC to traverse the micropore and the EI value smoothly approaches saturation; the MSC nucleus is a primary determinant of the MSC traversal dynamics through the micropores. In summary, the P-λ relationship can be divided into three parts according to the effect of the MSC membrane, as well as the combined effect of the MSC membrane and the MSC nucleus, and explains the specific factors that limit the deformation properties of MSCs when they pass through narrow channels of different sizes. These findings may contribute to understanding the mechanical properties of MSCs in their therapy.

The deformation of the shape of blood cells is a well-researched topic in single-cell biophysics. For instance, Xiao *et al.* simulated the dynamics of a single cell passing through a narrow slit to mimic the transmigration of circulating tumor cells. Li *et al.* simulated the dynamics of RBC passing through IES in the spleen. As the cells passed through the slits of a rectangular cross section, they displayed asymmetric deformations. In our earlier computational studies, we simulated the passage of age-associated RBCs through a splenic slit, and found that they had similar cell deformation patterns [79,80]. In contrast to the computational studies mentioned above, our present study simulates the traversal dynamics of an individual MSC through a narrow cleft with an alternative cross-sectional shape. Instead of the rectangular shape used in previous studies, the narrow cleft in our study has a circular cross section. Our simulation setup is uniformly symmetric. This leads to symmetric cell deformation along the circumference during the traversal of the MSC through the narrow cleft.

D. Effects of geometrical and mechanical properties of the MSC on its traversal dynamics

In this section, we systematically examine the impact of MSC geometrical and mechanical properties (includ-

ing cell-to-nucleus-diameter ratio, reduced cell volume, and cytoskeletal pre-stress states) on the traversal process.

First, we examine the effect of the cell-to-nucleus-diameter ratio, $\beta = \frac{D_{\text{MSC}}}{D_{\text{nucleus}}}$, by changing the values of D_{nucleus} from 9.75 to 11.29, 8.78, and 7.90 μm, while keeping the diameter of the MSC constant at $D_{\text{MSC}} = 15.8$ μm. Figure 3(a) shows the simulation results. Note that $\beta_0 = 1.62$ represents the original cell-to-nucleus-diameter ratio from the previous experiment [9]. It shows that the transit velocity of the MSC increases with the increase of β, both at low and high relative pressure differences. It is easy to understand why this occurs: when the β value increases, the diameter of the MSC nucleus reduces, lowering the flow resistance as the MSC passes through the micropores and increasing the transit velocity of the MSC. Next, we examine how the critical λ is impacted by the β parameter. The correlation between the critical λ and β parameter shows different trends at low and high relative pressure differences: at low relative pressure difference (e.g., 0.5), the critical λ value remains constant despite changes in the value of β; at high relative pressure difference (e.g., 1.0), it shows a different trend than at low relative pressure difference, namely, the critical value of λ increases as the value of β increases. The different trends can be attributed to the different roles played by the MSC membrane and the MSC nucleus at different relative pressure differences: at low relative pressure difference, the obtained λ is less than λ_{cutoff1}. As discussed in Secs. III B and III C, the deformation of the MSC membrane plays a decisive role in influencing the dynamics of MSC traversal, and the MSC nucleus hardly deforms in such a low λ region, as shown in Fig. 2(b). As β increases, the MSC nucleus decreases while the diameter of MSC is constant; hence, the critical λ ratio is almost constant regardless of the β changes. On the other hand, when the relative pressure difference increases to a high value (e.g., 1.0), the MSC nucleus begins to deform and assumes an increasingly crucial role in the traversal process compared to low relative pressure differences. The larger the β value, the smaller the diameter of the MSC nucleus. This, in turn,

facilitates the passage of the MSC through the micropore. Consequently, there is an increase in the critical λ value as β increases. This is also consistent with the simulation results in the Sec. III C, which shows that both the MSC membrane and MSC nucleus undergo significant deformation at the high λ region [Fig. 2(b)]. The critical λ smoothly approaches saturation with a further increase in β. As β increases in this regime, the critical λ remains largely unaffected since it has already reached a high value, equivalent to the critical size required for the MSC to pass through the micropore under a specific relative pressure difference of 1.0. This phenomenon is similar to our previous simulations of RBC traversal through narrow IESs [79,80]. To enable the MSC to pass through narrower micropores, a significantly higher relative pressure difference is necessary for further deformation.

Subsequently, we conducted multiple simulations to investigate the effect of reduced cell volume (v) on MSC traversal dynamics. Apart from the original value of $v_0 = 1.0$, we chose three other values of v, i.e., 0.97, 0.94, and 0.91, by increasing the cell surface area from 784.3 to 823.5, 862.7, and, finally, 901.9 μm^2, while keeping the cell volume ($V = 2065.2 \, \mu m^3$) constant. Figure 3(b) shows the MSC transit velocity and the critical λ ratio for different v values. The data suggest that the MSC transit velocity decreases with increasing v. It is widely known that the reduced cell volume would affect cell deformability. As the v value increases, the cell becomes more spherical, reducing cell deformability. As a result, the MSC transit time through the micropore is prolonged, leading to a decrease in the MSC transit velocity. Regarding the functional dependence of the critical λ ratio on v, it also shows a different trend at low and high relative pressure differences: the critical ratio of λ increases with decreasing v at low relative pressure differences (e.g., 0.5). As mentioned, a reduced v value would enhance the cell deformability. As a result, the MSC could pass through narrower micropores, increasing the λ ratio. However, it remains unaltered at high relative pressure differences (e.g., 1.0). In this scenario, the critical value of λ surpasses $\lambda_{cutoff2}$, where the MSC nucleus plays a crucial role in influencing the traversal dynamics of MSCs through the micropores. In this case, the diameter of the MSC nucleus does not change; thus, despite changes to v, the critical λ remains constant. AS v approaches 1, the cell deformability of the MSC membrane also contributes a non-negligible influence to the MSC traversal, causing a slight reduction in the critical λ ratio. These simulation results suggest that the reduced cell volume mainly determines the MSC traversal dynamics when the MSC nucleus does not deform or experiences negligible deformation. However, when the MSC nucleus undergoes large deformation, it significantly influences the traversal dynamics of MSCs through micropores.

Based on previous studies, the stress-free state refers to a three-dimensional geometry of the cytoskeleton in which there is no shear stress [60,81,82]. We consider several different simulation cases: an initial configuration in the unstressed state, three initial configurations under compressive stresses (corresponding to equilibrium bond length l_0 being 15%, 10%, and 5% shorter than the average initial bond length l_i), and three initial configurations under tensile stresses (corresponding to equilibrium bond lengths l_0 being 5%, 10%, and 15% longer than the average initial bond lengths l_i). We then

normalize these physical prestress values by using a specific value of $\tau_s = -0.60$ pN/μm, which corresponds to the shear stress at the point of maximum deformation of the MSC at $P = 0.5$. Figure 3(c) shows the correlation between the traversal velocity and the reduced prestress state of the cytoskeleton. When subjected to tensile stress, the MSC experiences higher tensile stress when passing through the micropore compared to being in a compressive state. As a result, the velocity of the MSC slows down as its initial tensile stress value increases. Conversely, the initial compressive stress of the MSC can offset a portion of the tensile stress during stretching, resulting in an increased transit velocity of the MSC. It is worth noting that alterations in the prestress state do not impact the critical λ parameter. This differs from the two other parameters (cell-to-nucleus-diameter ratio β and reduced cell volume v). Hence, we assert that the cell-to-nucleus-diameter ratio and reduced cell volume play more critical roles in MSC traversal.

In conclusion, the mesoscopic MSC model allows us to simulate and predict the effects of geometric parameters and cytoskeletal stress state on MSC passage through micropores, quantifying the importance of the role played by these factors in the process of MSC through narrow pores of different sizes, which is of great help in understanding the extravasation mechanism of MSC homing.

E. Shear strain characteristics of the MSC during its traversal through circular micropores

The shear strain at various time steps was calculated as an isolated MSC passed through the micropore. The equation for calculating the local shear strain γ during the MSC passage is as follows:

$$\gamma = \left\{ E_{xy}^2 + E_{xz}^2 + E_{yz}^2 + 1/6[(E_{xx} - E_{yy})^2 + (E_{xx} - E_{zz})^2 + (E_{yy} - E_{zz})^2] \right\}^{1/2},$$

where E_{mn} ($m, n = x, y, z$) is the component of the Green-Lagrangian strain tensor $\mathbf{E} = (\mathbf{F}^T\mathbf{F} - \mathbf{I})/2$. Here, $\mathbf{F} = \partial\mathbf{x}/\partial\mathbf{X} = \mathbf{I} + \partial\mathbf{u}/\partial\mathbf{X}$ is the deformation gradient tensor, where $\mathbf{I}$ is the identity matrix, and $\mathbf{x}, \mathbf{X}, \mathbf{u}$ are the instantaneous coordinates, initial coordinates, and displacement vectors of particles on the cell membrane, respectively. Figure 4 represents the local shear strain distributions of the MSC membrane and the MSC nucleus during cell passage under three different λ ratios (i.e., $\lambda = 1.13, 1.39,$ and 1.58). The following presents the shared characteristics of the shear stresses: As the MSC approaches the micropore, its front end protrudes and experiences the highest shear strain. When half of the MSC enters the micropore, the tail bulges out and the shear strain gradually increases. When the whole MSC enters the micropore, the maximum shear strain occurs at the back of the cell. Afterwards, the MSC promptly exits the micropore and returns to its original shape, causing the local shear strain to return to zero. Particularly at $\lambda = 1.13$, a small relative pressure difference could drive the MSC to pass through the micropore, causing a slight cell deformation that encounters a maximum shear strain of about 0.8 [Fig. 4(a)]. In this situation, the distance between the MSC membrane and its nucleus is noticeably far apart. As λ increases to 1.39,
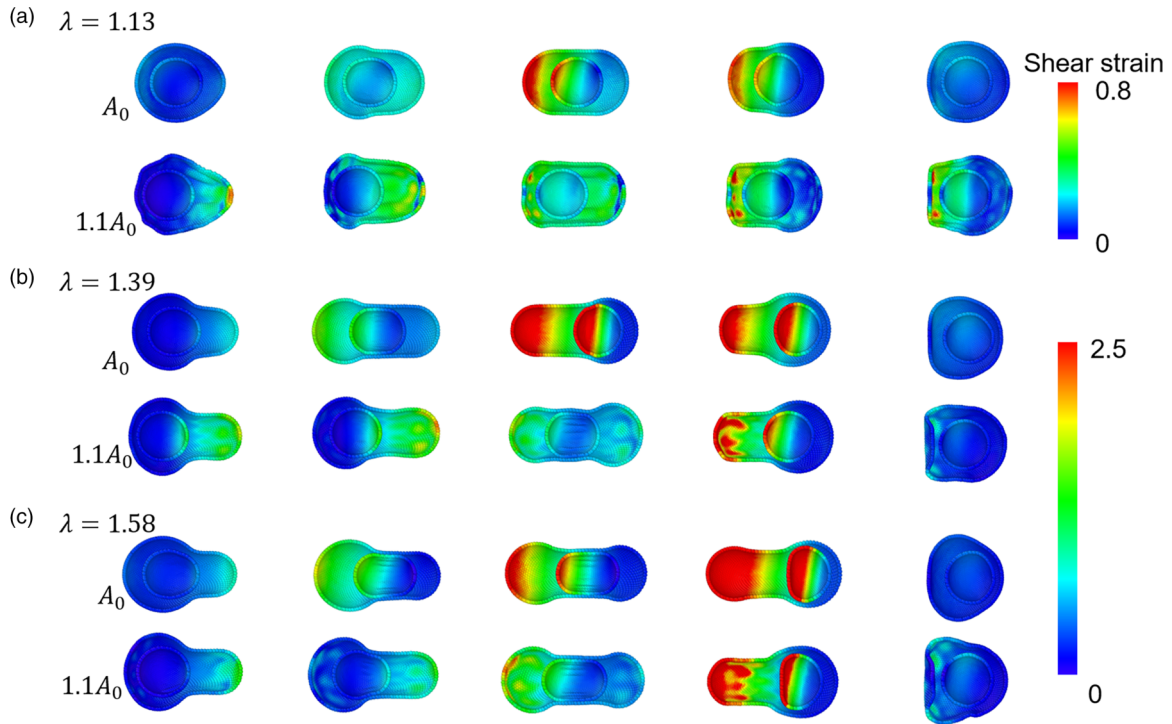
FIG. 4. Temporal snapshots of shear strain distributions of MSC membrane (outer contour) and MSC nucleus (inner contour) as the whole MSC passes through the micropore under λ ratio = (a) 1.13, (b) 1.39, and (c) 1.58. In each subfigure, the symbols A_0 and $1.1A_0$ represent the whole MSC with its original membrane surface area (A_0) and the expanded MSC by increasing its surface area by 10% ($1.1A_0$).

the MSC passes through a narrower micropore, resulting in greater deformation of the anterior part of the MSC compared to that at $\lambda = 1.13$, as shown in Fig. 4(b). Additionally, the MSC nucleus experiences significant deformation. As the λ ratio reaches 1.58, the MSC passes through a progressively narrower micropore. This results in the need for a much higher relative pressure difference (e.g., $P = 1.0$) to force the MSC through the micropore, leading to a maximum shear strain of 2.5 at this stage [see Fig. 4(c)]. Different distributions of cell shear strain can aid in the comprehension of the underlying mechanisms of cell membrane vesiculation and cell rupture during cell traversal processes.

Research has demonstrated that the surface area of the cell membrane significantly impacts cell deformability [22,48,79,83]. Previous experimental studies have observed that circulating cells utilize the endomembrane to remodel their plasma membrane continually, thereby increasing the total membrane area without altering their shape [84]. Here, we examine how changes in cell surface area can affect cell behavior. Specifically, our simulation expands the MSC's surface area to $1.1A_0$ by increasing the membrane surface area by 10%. Compared to the MSC with A_0 membrane surface area, the expanded MSC demonstrates increased cell membrane deformability, resulting in changes in cell shape deformation and local shear stress distributions. Our analysis of shear strain contours reveals that the expanded MSC always experiences less severe shear strains than the original MSC. This suggests that increasing the surface area of MSC may help to reduce the cell membrane damage (e.g., cell lysis) during passage through narrow passages.

F. Velocity analysis of the MSC during its traversal through circular micropores

A direct means of triggering the motion of individual MSCs is possible by analyzing the instantaneous velocity variations of individual MSCs during their traversal processes. To facilitate analysis, we analyze the velocities of the center of mass of the whole MSC and its main components, the MSC nucleus and membrane, during their traversal processes under three different λ ratios ($\lambda = 1.13$, 1.39, and 1.58), as depicted in Fig. 5(a). When $\lambda = 1.13$, the MSC nucleus passes easily through the micropore without deceleration, reaching a maximum velocity of $3300 \, \mu m/s$. In contrast, the velocity profiles of the whole MSC and pure MSC membrane are slower during their traversal processes. When $\lambda = 1.39$ or 1.58, the velocity profiles of the whole MSC and its main components (i.e., the MSC nucleus and the pure MSC membrane) were divided into three distinct stages: (1) a deceleration stage when the whole MSC, MSC nucleus, or pure MSC membrane moves closer to the micropore, (2) an acceleration stage when the center of mass of the whole MSC, MSC nucleus, or pure MSC membrane enters (or has entered) the micropore, and (3) a second deceleration stage when the whole body of the whole MSC, MSC nucleus, or pure MSC membrane leaves the micropore. In addition, at $\lambda = 1.58$, the pure MSC membrane exhibited higher velocities in stage 2 compared to the whole MSC, suggesting that the MSC nucleus plays an important role in the process of MSC traversal at a high λ ratio. These findings are consistent with those shown in Fig. 2(a).

As a cell passes through micropores of varying size, the velocity of the fluid flow surrounding the cell undergoes
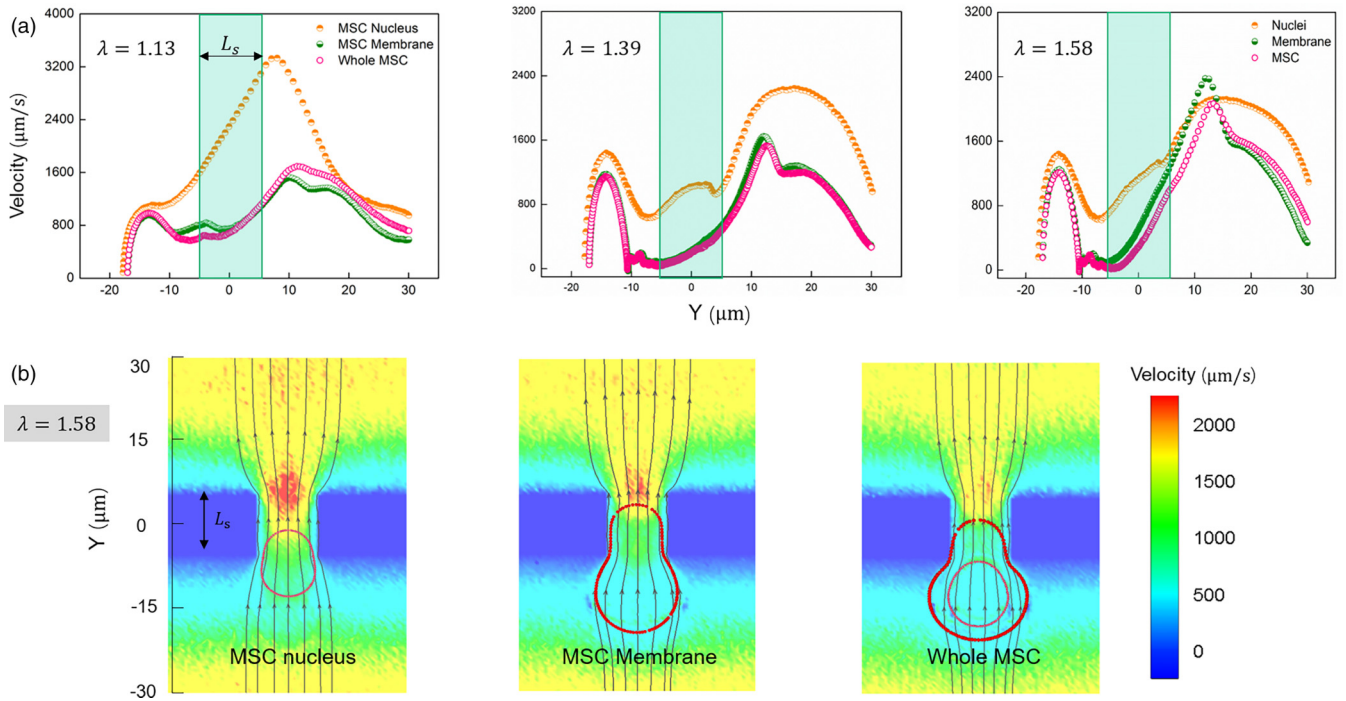
FIG. 5. (a) Velocity profiles of the MSC nucleus, MSC membrane, and the whole MSC during their dynamic traversing processes. The orange circles represent the velocity of the center of mass of the MSC nucleus, the green circles represent the velocity of the MSC membrane, and the pink circles represent the velocity of the whole MSC. (b) Flow streamlines and flow contours of the suspending fluid around the MSC nucleus, MSC membrane, and whole MSC at $\lambda = 1.58$. In the figure, each arrow represents the direction of the fluid flow velocity; the flow contour of the velocity field is shown with the velocity in the range between 0 and 2000 μm/s, and it takes different colors depending on the magnitude of the fluid flow velocity. The middle regions with the red lines indicate the presence of the MSC nucleus, MSC membrane, and whole MSC, respectively.

significant changes. Figure 5(b) illustrates flow streamlines as well as two-dimensional velocity contours over the xy cross section under considerable confinement (i.e., $\lambda = 1.58$). The diameters of the whole MSC and its two components (the MSC nucleus and the pure MSC membrane) are all larger than the micropore at $\lambda = 1.58$; therefore, shape deformation occurs as they enter the micropore, which, in turn, affects the surrounding fluid flow field. In particular, for the simulation of the MSC nucleus, its diameter is only 1.026 times larger than that of the micropore, making its influence on the local flow field minimal. Consequently, the flow streamline profile in front of the micropore is virtually symmetrical to that behind the micropore. However, in the simulation case of the whole MSC (or the pure MSC membrane), the diameter is approximately 1.58 times larger than that of the micropore, resulting in significant shape deformation when the cell passes through the micropore. The deformed MSC or the pure MSC membrane can significantly influence the flow of surrounding fluid, leading to a reduction in the approaching velocity of the MSC as it reaches the micropore entrance [see the rightmost subfigure in Fig. 5(a)]. As per Fig. 5(b), it shows no zero velocity fluctuations over the solid wall surface, which may be attributed to Brownian motion and random thermal fluctuations caused by the coarse-graining procedure. The DPD approach indicates that thermal fluctuations in DPD fluids increase with the level of coarse graining [85]. This study takes special care in the DPD simulation of fluid flow to eliminate particle density fluctuations and maintain a no-slip

boundary condition. As discussed in Sec. III A, despite slight velocity variations, the differences between the DPD and continuum simulation results are negligible (see Fig. S3 in the Supplemental Material [7]). Accordingly, the application of the modified DPD method to fluid flow is feasible.

G. Functional dependence of the critical ratio λ on micropore length

To determine the influence of micropore length on MSC traversal dynamics, we conducted a series of simulations for MSC traversal through circular micropores. These simulations were performed with and without consideration of the MSC nucleus by changing the micropore length along the flow direction (L_s). We chose L_s values of 2, 4, 6, 8, and 11 μm in the DPD simulations. Figure 6(a) displays the simulation results. The results show that the critical λ_{cutoff} ratio decreases with increasing L_s when L_s is less than 8 μm. However, the λ_{cutoff} ratio remains constant for $L_s \geqslant 8$ μm. The comparison of the whole MSC and the pure MSC membrane results in Fig. 6(a) reveals that the MSC nucleus plays a crucial role in determining the critical λ value. The shape of the MSC membrane and the MSC nucleus is presented in Fig. 6(b), where the whole MSC passes through the micropores with lengths of $L_s = 2$ μm [Fig. 6(b)(upper)] and 6 μm [Fig. 6(b)(lower)]. By comparing these figures, it is evident that the micropore length determines the extended size of the neck portions of the MSC, leading to various degrees of cell deformation. This
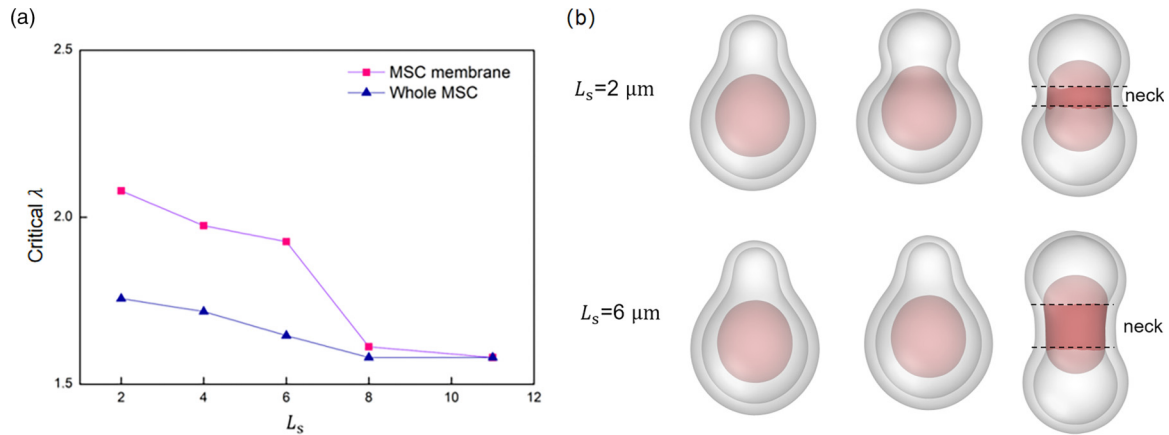
FIG. 6. (a) The functional dependence of critical ratio λ on the pore length L_s. The purple squares and the blue triangles represent the simulation data for the MSC membrane and the whole MSC, respectively. (b) Shape deformation of the whole MSC during its passage through the micropores with $L_s = 2\,\mu m$ (upper) and $6\,\mu m$ (lower), respectively.

is characterized by the EI values of 2.5 for the case with $L_s = 2\,\mu m$ and 3.0 for the case with $L_s = 6\,\mu m$.

IV. CONCLUSION

A better understanding of how MSCs overcome the mechanical constraints and limitations of their three-dimensional (3D) environment is of great importance for MSC-based therapies. This paper showcases the unique capabilities and advantages of using multiscale simulations to characterize the complex dynamic behavior of individual MSCs in an IEC-like microenvironment. First, we perform systematic computational simulations based on previous microfluidic experiments that provided *in vitro* quantitative information on MSC dynamics [9] to investigate the cell traversal behavior under different sizes of IEC-like micropores and elucidate the underlying mechanisms. Second, we quantify the shape changes and conduct a mechanical evaluation of individual MSCs, focusing on the isolated and combined influence of the MSC membrane and nucleus on the processes of cell traversal. Finally, we investigate how changes in micropore length lead to modifications in the MSC passages. The predictive computational simulations reveal the effects of micropore length and MSC nucleus on the traversal dynamics of individual MSCs. As individual MSCs travel through narrow passages at the single-cell level, the simulations provide a quantitative measure of the deformation and dynamics.

The current MSC model can simulate the mechanics of MSC traversal through narrow clefts. However, it does not account for the adhesion interactions between cells. As a result, it cannot simulate the initial step of MSC systemic homing, which involves cell attachment to and deceleration on the vessel wall via selectin-mediated interactions. These limitations can be overcome by combining the current DPD-based

MSC model with a stochastic catch-bond-mediated model for cell adhesion, covering both molecular and cellular scales. Furthermore, to enhance the reliability of future predictions based on the hybrid MSC model, it is crucial to validate it computationally and perform extensive tests against independent experiments. The simulations with the hybrid model would help one to study the multistep processes involved in MSC homing dynamics.

[1] D. G. Phinney and D. J. Prockop, Concise review: Mesenchymal stem/multipotent stromal cells: The state of transdifferentiation and modes of tissue repair—Current views, Stem Cells **25**, 2896 (2007).

[2] J. Ankrum and J. M. Karp, Mesenchymal stem cell therapy: Two steps forward, one step back, Trends Mol. Med. **16**, 203 (2010).

[3] J. M. Karp and G. S. Leng Teo, Mesenchymal stem cell homing: The devil is in the details, Cell Stem Cell **4**, 206 (2009).

[4] G. S. Teo, J. A. Ankrum, R. Martinelli, S. E. Boetto, K. Simms, T. E. Sciuto, A. M. Dvorak, J. M. Karp, and C. V. Carman, Mesenchymal stem cells transmigrate between and directly through tumor necrosis factor-α-activated endothelial cells via both leukocyte-like and novel mechanisms, Stem Cells **30**, 2472 (2012).

[5] V. F. Segers, I. Van Riet, L. J. Andries, K. Lemmens, M. J. Demolder, A. J. De Becker, M. M. Kockx, and G. W. De Keulenaer, Mesenchymal stem cell adhesion to cardiac microvascular endothelium: Activators and mechanisms, Am. J. Physiol. Heart Circ. Physiol. **290**, H1370 (2006).

[6] B. Rüster, S. Göttig, R. J. Ludwig, R. Bistrian, S. Müller, E. Seifried, J. Gille, and R. Henschler, Mesenchymal stem cells display coordinated rolling and adhesion behavior on endothelial cells, Blood **108**, 3938 (2006).

[7] See Supplemental Material at http://link.aps.org/supplemental/10.1103/PhysRevE.108.054402 for a file containing supplementary text and figures as references in the main text. The file Video S1.mp4 is a video providing a computational simulation of a whole individual MSC passing through the IEC-like micropore (Video S1). The modeled whole MSC consists of an MSC membrane (rendered in white) and an MSC nucleus (rendered in red), and the IEC-like micropore is rendered in green.

[8] P. M. Davidson, J. Sliz, P. Isermann, C. Denais, and J. Lammerding, Design of a microfluidic device to quantify dynamic intra-nuclear deformation during cell migration through confining environments, Integr. Biol. **7**, 1534 (2015).

[9] H. H. Lipowsky, D. T. Bowers, B. L. Banik, and J. L. Brown, Mesenchymal stem cell deformability and implications for microvascular sequestration, Ann. Biomed. Eng. **46**, 640 (2018).

[10] B. Weigelin, G.-J. Bakker, and P. A. Friedl, Intravital third harmonic generation microscopy of collective melanoma cell invasion, IntraVital **1**, 32 (2012).

[11] T. E. Angelini, E. Hannezo, X. Trepat, J. J. Fredberg, and D. A. Weitz, Cell migration driven by cooperative substrate deformation patterns, Phys. Rev. Lett. **104**, 168104 (2010).

[12] S. Pillay, H. M. Byrne, and P. K. Maini, Modeling angiogenesis: A discrete to continuum description, Phys. Rev. E **95**, 012410 (2017).

[13] H. W. Hou, A. A. S. Bhagat, A. G. Lin Chong, P. Mao, K. S. Wei Tan, J. Han, and C. T. Lim, Deformability based cell margination—A simple microfluidic design for malaria-infected erythrocyte separation, Lab Chip **10**, 2605 (2010).

[14] A. A. S. Bhagat, H. W. Hou, L. D. Li, C. T. Lim, and J. Han, Pinched flow coupled shear-modulated inertial microfluidics for high-throughput rare blood cell separation, Lab Chip **11**, 1870 (2011).

[15] Q. Guo, S. M. McFaul, and H. Ma, Deterministic microfluidic ratchet based on the deformation of individual cells, Phys. Rev. E **83**, 051910 (2011).

[16] T. Ye, N. Phan-Thien, C. T. Lim, L. Peng, and H. Shi, Hybrid smoothed dissipative particle dynamics and immersed boundary method for simulation of red blood cells in flows, Phys. Rev. E **95**, 063314 (2017).

[17] T. Tao, Y. Wang, W. Chen, Z. Li, W. Su, Y. Guo, P. Deng, and J. Qin, Engineering human islet organoids from iPSCs using an organ-on-chip platform, Lab Chip **19**, 948 (2019).

[18] Y. Qiang, J. Liu, M. Dao, S. Suresh, and E. Du, Mechanical fatigue of human red blood cells, Proc. Natl. Acad. Sci. USA **116**, 19828 (2019).

[19] Y. Qiang, J. Liu, M. Dao, and E. Du, In vitro assay for single-cell characterization of impaired deformability in red blood cells under recurrent episodes of hypoxia, Lab Chip **21**, 3458 (2021).

[20] J. P. Shelby, J. White, K. Ganesan, P. K. Rathod, and D. T. Chiu, A microfluidic model for single-cell capillary obstruction by plasmodium falciparum-infected erythrocytes, Proc. Natl. Acad. Sci. USA **100**, 14618 (2003).

[21] H. Bow, I. V. Pivkin, M. Diez-Silva, S. J. Goldfless, M. Dao, J. C. Niles, S. Suresh, and J. Han, A microfabricated deformability-based flow cytometer with application to malaria, Lab Chip **11**, 1065 (2011).

[22] D. J. Quinn, I. Pivkin, S. Y. Wong, K. H. Chiam, M. Dao, G. E. Karniadakis, and S. Suresh, Combined simulation and experimental study of large deformation of red blood cells in microfluidic systems, Ann. Biomed. Eng. **39**, 1041 (2011).

[23] L. Shi, T.-W. Pan, and R. Glowinski, Deformation of a single red blood cell in bounded poiseuille flows, Phys. Rev. E **85**, 016307 (2012).

[24] P. Preira, V. Grandné, J.-M. Forel, S. Gabriele, M. Camara, and O. Theodoly, Passive circulating cell sorting by deformability using a microfluidic gradual filter, Lab Chip **13**, 161 (2013).

[25] E. Du, M. Diez-Silva, G. J. Kato, M. Dao, and S. Suresh, Kinetics of sickle cell biorheology and implications for painful vasoocclusive crisis, Proc. Natl. Acad. Sci. USA **112**, 1422 (2015).

[26] D. P. Papageorgiou, S. Z. Abidi, H.-Y. Chang, X. Li, G. J. Kato, G. E. Karniadakis, S. Suresh, and M. Dao, Simultaneous polymerization and adhesion under hypoxia in sickle cell disease, Proc. Natl. Acad. Sci. USA **115**, 9473 (2018).

[27] D.-H. Lee, X. Li, N. Ma, M. A. Digman, and A. P. Lee, Rapid and label-free identification of single leukemia cells from blood in a high-density microfluidic trapping array by fluorescence lifetime imaging microscopy, Lab Chip **18**, 1349 (2018).

[28] O. Forouzan, J. M. Burns, J. L. Robichaux, W. L. Murfee, and S. S. Shevkoplyas, Passive recruitment of circulating leukocytes into capillary sprouts from existing capillaries in a microfluidic system, Lab Chip **11**, 1924 (2011).

[29] J. B. Freund, Numerical simulation of flowing blood cells, Annu. Rev. Fluid Mech. **46**, 67 (2014).

[30] Y. Liu, Q. Yang, L. Cao, and F. Xu, Analysis of leukocyte behaviors on microfluidic chips, Adv. Healthc. Mater. **8**, 1801406 (2019).

[31] T. H. Schreiber, V. Shinder, D. W. Cain, R. Alon, and R. Sackstein, Shear flow-dependent integration of apical and subendothelial chemokines in T-cell transmigration: Implications for locomotion and the multistep paradigm, Blood **109**, 1381 (2007).

[32] G. P. Downey and G. S. Worthen, Neutrophil retention in model capillaries: Deformability, geometry, and hydrodynamic forces, J. Appl. Physiol. **65**, 1861 (1988).

[33] S. Sormendi, M. Deygas, A. Sinha, M. Bernard, A. Krüger, I. Kourtzelis, G. Le Lay, P. J. Sáez, M. Gerlach, K. Franke, A. Meneses, M. Krater, A. Palladini, J. Guck, U. Coskun, T. Chavakis, P. Vargas, and B. Wielockx, HIF2α is a direct regulator of neutrophil motility, Blood **137**, 3416 (2021).

[34] P. Vajkoczy, S. Blum, M. Lamparter, R. Mailhammer, R. Erber, B. Engelhardt, D. Vestweber, and A. K. Hatzopoulos, Multistep nature of microvascular recruitment of *Ex Vivo*-expanded

embryonic endothelial progenitor cells during tumor angiogenesis, J. Expt. Med. **197**, 1755 (2003).

[35] M. Xavier, P. Rosendahl, M. Herbig, M. Kräter, D. Spencer, M. Bornhäuser, R. O. Oreffo, H. Morgan, J. Guck, and O. Otto, Mechanical phenotyping of primary human skeletal stem cells in heterogeneous populations by real-time deformability cytometry, Integr. Biol. **8**, 616 (2016).

[36] C. Toma, W. R. Wagner, S. Bowry, A. Schwartz, and F. Villanueva, Fate of culture-expanded mesenchymal stem cells in the microvasculature: *In vivo* observations of cell kinetics, Circ. Res. **104**, 398 (2009).

[37] S. K. Doddi and P. Bagchi, Three-dimensional computational modeling of multiple deformable cells flowing in microvessels, Phys. Rev. E **79**, 046318 (2009).

[38] P. Van Liedekerke, E. Tijskens, H. Ramon, P. Ghysels, G. Samaey, and D. Roose, Particle-based model to simulate the micromechanics of biological cells, Phys. Rev. E **81**, 061906 (2010).

[39] X. Li, P. M. Vlahovska, and G. E. Karniadakis, Continuum- and particle-based modeling of shapes and dynamics of red blood cells in health and disease, Soft Matter **9**, 28 (2013).

[40] D. S. Hariprasad and T. W. Secomb, Prediction of noninertial focusing of red blood cells in poiseuille flow, Phys. Rev. E **92**, 033008 (2015).

[41] G. Gompper and D. A. Fedosov, Modeling microcirculatory blood flow: Current state and future perspectives, Wiley Interdiscip. Rev. Syst. Biol. Med. **8**, 157 (2016).

[42] T. Ye, N. Phan-Thien, and C. T. Lim, Particle-based simulations of red blood cells—A review, J. Biomech. **49**, 2255 (2016).

[43] X. Li, H. Li, H.-Y. Chang, G. Lykotrafitis, and G. E. Karniadakis, Computational biomechanics of human red blood cells in hematological disorders, J. Biomech. Eng. **139**, 021008 (2017).

[44] T. W. Secomb, Blood flow in the microcirculation, Annu. Rev. Fluid Mech. **49**, 443 (2017).

[45] I. Lavi, N. Meunier, R. Voituriez, and J. Casademunt, Motility and morphodynamics of confined cells, Phys. Rev. E **101**, 022404 (2020).

[46] J. B. Freund, The flow of red blood cells through a narrow spleen-like slit, Phys. Fluids **25**, 110807 (2013).

[47] H. Lu and Z. Peng, Boundary integral simulations of a red blood cell squeezing through a submicron slit under prescribed inlet and outlet pressures, Phys. Fluids **31**, 031902 (2019).

[48] I. V. Pivkin, Z. Peng, G. E. Karniadakis, P. Buffet, M. Dao, and S. Suresh, Biomechanics of red blood cells in human spleen and consequences for physiology and disease, Proc. Natl. Acad. Sci. USA **113**, 7804 (2016).

[49] H. Li, L. Lu, X. Li, P. Buffet, M. Dao, G. E. Karniadakis, and S. Suresh, Mechanics of diseased red blood cells in human spleen and consequences for hereditary blood disorders, Proc. Natl. Acad. Sci. USA **115**, 9574 (2018).

[50] X. Li, E. Du, M. Dao, S. Suresh, and G. E. Karniadakis, Patient-specific modeling of individual sickle cell behavior under transient hypoxia, PLOS Comput. Biol. **13**, e1005426 (2017).

[51] P. J. Hoogerbrugge and J. M. V. A. Koelman, Simulating microscopic hydrodynamic phenomena with dissipative particle dynamics, Europhys. Lett. **19**, 155 (1992).

[52] H. Lei, B. Caswell, and G. E. Karniadakis, Direct construction of mesoscopic models from microscopic simulations, Phys. Rev. E **81**, 026704 (2010).

[53] P. Español, Dissipative particle dynamics for a harmonic chain: A first-principles derivation, Phys. Rev. E **53**, 1572 (1996).

[54] M. P. Allen and D. J. Tildesley, *Computer Simulation of Liquids* (Oxford University Press, Oxford, 2017).

[55] I. Titushkin and M. Cho, Distinct membrane mechanical properties of human mesenchymal stem cells determined using laser optical tweezers, Biophys. J. **90**, 2582 (2006).

[56] S. Ma, S. Wang, X. Qi, K. Han, X. Jin, Z. Li, G. Hu, and X. Li, Multiscale computational framework for predicting viscoelasticity of red blood cells in aging and mechanical fatigue, Comput. Methods. Appl. Mech. Eng. **391**, 114535 (2022).

[57] K. Zhang, Z. Li, and S. Chen, Analytical prediction of electrowetting-induced jumping motion for droplets on hydrophobic substrates, Phys. Fluids **31**, 081703 (2019).

[58] R. B. Koneru, A. Flatau, Z. Li, L. Bravo, M. Murugan, A. Ghoshal, and G. E. Karniadakis, Quantifying the dynamic spreading of a molten sand droplet using multiphase mesoscopic simulations, Phys. Rev. Fluids **7**, 103602 (2022).

[59] D. R. Gossett, H. T. K. Tse, S. A. Lee, Y. Ying, A. G. Lindgren, O. O. Yang, and J. Rao, Hydrodynamic stretching of single cells for large population mechanical phenotyping, Proc. Natl. Acad. Sci. **109**, 7630 (2012).

[60] Z. Peng, X. Li, I. V. Pivkin, M. Dao, G. E. Karniadakis, and S. Suresh, Lipid bilayer and cytoskeletal interactions in a red blood cell, Proc. Natl. Acad. Sci. USA **110**, 13356 (2013).

[61] H. Lei, D. A. Fedosov, B. Caswell, and G. E. Karniadakis, Blood flow in small tubes: Quantifying the transition to the noncontinuum regime, J. Fluid Mech. **722**, 214 (2013).

[62] T. Ye, N. Phan-Thien, C. T. Lim, and Y. Li, Red blood cell motion and deformation in a curved microvessel, J. Biomech. **65**, 12 (2017).

[63] G. Li, T. Ye, S. Wang, X. Li, and R. Ui Haq, Numerical design of a highly efficient microfluidic chip for blood plasma separation, Phys. Fluids **32**, 031903 (2020).

[64] M. Dao, J. Li, and S. Suresh, Molecularly based analysis of deformation of spectrin network and human erythrocyte, Mater. Sci. Eng. C **26**, 1232 (2006).

[65] I. V. Pivkin and G. E. Karniadakis, Accurate coarse-grained modeling of red blood cells, Phys. Rev. Lett. **101**, 118105 (2008).

[66] D. A. Fedosov, B. Caswell, and G. E. Karniadakis, A multiscale red blood cell model with accurate mechanics, rheology, and dynamics, Biophys. J. **98**, 2215 (2010).

[67] G. Li, Y. Qiang, H. Li, X. Li, M. Dao, and G. E. Karniadakis, *In silico* and *in vitro* study of the adhesion dynamics of erythrophagocytosis in sickle cell disease, Biophys. J. **122**, 2590 (2023).

[68] W. Helfrich, Elastic properties of lipid bilayers: Theory and possible experiments, Z. Naturforsch., C, J. Biosci. **28**, 693 (1973).

[69] G. Gompper and D. M. Kroll, Random surface discretization and the renormalization of the bending rigidity, J. Phys. I France **6**, 1305 (1996).

[70] H. Wang, C. N. Alarcón, B. Liu, F. Watson, S. Searles, C. K. Lee, J. Keys, W. Pi, D. Allen, J. Lammerding, J. D. Bui, and R. L. A. Klemke, Genetically engineered and enucleated human mesenchymal stromal cells for the targeted delivery

of therapeutics to diseased tissue, Nat. Biomed. Eng. **6**, 882 (2021).

[71] N. Caille, O. Thoumine, Y. Tardy, and J. J. Meister, Contribution of the nucleus to the mechanical properties of endothelial cells, J. Biomech. **35**, 177 (2002).

[72] F. Guilak, J. R. Tedrow, and R. Burgkart, Viscoelastic properties of the cell nucleus, Biochem. Biophys. Res. Commun. **269**, 781 (2000).

[73] P. J. Stewart-Hutchinson, C. M. Hale, D. Wirtz, and D. Hodzic, Structural requirements for the assembly of LINC complexes and their function in cellular mechanical stiffness, Expt. Cell Res. **314**, 1892 (2008).

[74] J. Lammerding, Mechanics of the nucleus, Compr. Physiol. **1**, 783 (2011).

[75] S. Plimpton, Fast parallel algorithms for short-range molecular dynamics, J. Comput. Phys. **117**, 1 (1995).

[76] W. Pan, B. Caswell, and G. E. Karniadakis, Rheology, microstructure and migration in Brownian colloidal suspensions, Langmuir **26**, 133 (2010).

[77] J. Guo, X. Li, Y. Liu, and H. Liang, Flow-induced translocation of polymers through a fluidic channel: A dissipative particle dynamics simulation study, J. Chem. Phys. **134**, 134906 (2011).

[78] M. Braide, U. Nannmark, and U. Bagge, Bolus filtration of leukocytes: A method to study the pressure dependence of leukocyte filter pore passage time distributions, Clin. Hemorheol. Microcirc. **11**, 369 (1991).

[79] X. Qi, S. Wang, S. Ma, K. Han, and X. Li, Quantitative prediction of flow dynamics and mechanical retention of surface-altered red blood cells through a splenic slit, Phys. Fluids **33**, 051902 (2021).

[80] S. Ma, X. Qi, K. Han, S. Wang, G. Hu, and X. Li, Computational investigation of flow dynamics and mechanical retention of age-associated red blood cells in the spleen, Phys. Rev. Fluids **8**, 063103 (2023).

[81] Z. Peng, A. Mashayekh, and Q. Zhu, Erythrocyte responses in low-shear-rate flows: Effects of non-biconcave stress-free state in the cytoskeleton, J. Fluid Mech. **742**, 96 (2014).

[82] Z. Peng, R. J. Asaro, and Q. Zhu, Multiscale simulation of erythrocyte membranes, Phys. Rev. E **81**, 031904 (2010).

[83] I. Safeukui, P. A. Buffet, G. Deplaine, S. Perrot, V. Brousse, A. Ndour, M. Nguyen, O. Mercereau-Puijalon, P. H. David, G. Milon, and N. Mohandas, Quantitative assessment of sensing and sequestration of spherocytic erythrocytes by the human spleen, Blood **120**, 424 (2012).

[84] C. E. Morris and U. Homann, Cell surface area regulation and membrane tension, J. Membr. Biol. **179**, 79 (2001).

[85] I. V. Pivkin and G. E. Karniadakis, Controlling density fluctuations in wall-bounded dissipative particle dynamics systems, Phys. Rev. Lett. **96**, 206001 (2006).